Materials Characterization 175 (2021) 111044

Contents lists available at ScienceDirect

Materials Characterization

journal homepage: www.elsevier.com/locate/matchar

Texture development and dislocation activities in Mg-Nd and Mg-Ca alloy sheets

C. Ha [a,*], J. Bohlen [a,*], X. Zhou [b], H.-G. Brokmeier [b], K.U. Kainer [a,c], N. Schell [d], D. Letzig [a], S. Yi [a,*]

[a] Magnesium Innovation Centre (MagIC), Institute of Materials and Process Design, Helmholtz-Zentrum Geesthacht, Max-Planck-Str. 1, D-21502 Geesthacht, Germany
[b] Institute of Materials Science and Engineering (IWW), Clausthal University of Technology, Agricolastr. 6, D-38678, Clausthal-Zellerfeld, Germany
[c] Chair of Light Elements Engineering, Foundry and Automation, Wrocław University of Science and Technology, W. Wyspianskiego 27, 50-370 Wrocław, Poland
[d] HZG Outstation at DESY, Helmholtz-Zentrum Geesthacht, Notkestr. 85, D-22607 Hamburg, Germany

ARTICLE INFO

Keywords:
Magnesium alloys
Tensile test
Texture
Dislocation
X-ray analysis

ABSTRACT

Texture modification during sheet rolling appears differently in binary Mg-RE (rare-earth) or Mg-Ca alloy, compared to their ternary counterparts containing Zn. The differences in texture development and the active deformation mechanisms under tensile loading were investigated in the binary alloys. These analyses are based on in-situ synchrotron experiments and electron backscatter diffraction measurements to reveal direct experimental evidence of the texture development and the active deformation mechanisms. Higher activations of nonbasal <a> and pyramidal <c+a> dislocations were found in the Nd or Ca containing Mg alloys, compared to the Mg-Zn alloy. The texture development shows an obvious feature, which is a broadening of the basal pole intensity distribution perpendicular to the loading direction and a strengthening of the $<10\bar{1}0>$ pole at the loading direction in all examined sheets. This texture development relates to the higher activation of prismatic <a> slip. The addition of Zn in the Mg-RE or Mg-Ca alloys further promotes the activation of nonbasal <a> and pyramidal <c+a> dislocations. This enhanced prismatic <a> slip in the Zn containing ternary alloys is confirmed by EBSD misorientation analysis.

1. Introduction

The improved formability of certain Mg sheet alloys containing rare earth (RE) elements or Ca is associated with a texture modification during thermomechanical processing, i.e. the sheet rolling and subsequent annealing process [1–4]. Such texture modification is found in rolled sheets with a randomized orientation distribution compared to those in classical Mg alloy sheets, e.g. AZ31. Several mechanisms have been associated with the effect of alloying elements and the development of specific texture components, represented by a basal pole split toward the rolling direction (RD) or a basal pole broadened toward the transverse direction (TD). It has been revealed by crystal-plasticity simulation that the basal pole spread toward the RD is related to the activation of pyramidal II <c+a> slip systems [1]. The basal pole broadening toward the TD has been associated with a large amount of twinning and the respective orientation changes of the matrix grains [4,5], as well as with the enhanced activation of prismatic <a> slip in ternary Mg-Zn-RE alloys [6]. Furthermore, the varying impact of different recrystallization mechanisms has also conclusively been suggested to explain such texture development, e.g. by particle-simulated nucleation [7], shear band nucleation [8], or boundary pinning [9]. Earlier studies regarding the texture weakening investigated the deformation or recrystallization mechanisms either in binary, e.g. Mg-RE or Mg-Ca alloys, or their ternary counterparts containing Zn, Al, or Mn. In our previous work, the impact of additional Nd and Ca in a binary Mg-Zn alloy was investigated at various temperatures. Enhanced activity of nonbasal <a> dislocations due to the addition of Nd or Ca was related to the texture development with the basal pole spread to the TD under tensile loading [6]. However, the binary Mg alloys containing Y, Ce, Nd, or Ca show a spread of the basal pole toward the RD [6,10–12].

It is, therefore, necessary to evaluate the influence of individual alloying elements on the deformation and RX mechanisms that result in different texture development. Only through such an approach, the exact influence of the individual alloying element can be unveiled. Besides, the deformation mechanisms, which cause rotation of grains toward random orientations, are closely correlated to recrystallization

* Corresponding authors.
E-mail addresses: changwan.ha@hzg.de (C. Ha), jan.bohlen@hzg.de (J. Bohlen), sangbong.yi@hzg.de (S. Yi).

https://doi.org/10.1016/j.matchar.2021.111044
Received 14 August 2020; Received in revised form 12 February 2021; Accepted 11 March 2021
Available online 13 March 2021

mechanisms. Advanced experimental techniques and evaluation methods promote an understanding of the crucial mechanisms that contribute to the texture and microstructure developments in Mg alloys. The recently developed experimental techniques allow an investigation of the texture development and the dislocation structure in real-time under various conditions, e.g. a representative deformation condition or dynamic and static recrystallization.

In the present study, binary Mg-Nd and Mg-Ca alloys were examined to reveal the activities of different deformation mechanisms using two experimental analysis approaches, i.e. convolutional multiple whole profile (CMWP) fitting procedure and in-grain misorientation axes (IGMA) analyses. The results obtained from the binary alloys were analyzed in comparison to their ternary counterparts containing Zn, i.e. Mg-Zn-Nd, and Mg-Zn-Ca alloys. The binary Mg-Zn is used as a reference alloy without RE or Ca addition. The quantitative analysis of the active deformation modes and the identification of the predominant dislocation slip modes using in-situ experiments for different Mg alloys were successfully conducted in conjunction with the CMWP and IGMA analyses. Moreover, as sheets with different textures were obtained, which itself will influence the activity of the deformation mechanisms, the in-situ measurements were conducted and compared in the RD and TD of the sheets to estimate the intrinsic effect of the alloy composition on the dislocation activities, rather than the impact of the initial texture. The experimental results obtained in the present study provide a meaningful pathway to understand the interrelation among the initial texture in terms of alloy compositions, the active deformation modes, and their contribution to the microstructure and texture evolution during thermomechanical treatments.

2. Materials and methods

2.1. Materials

Binary and ternary Mg alloys of 5 different compositions, see Table 1, were gravity cast and machined to slabs with 20 mm in thickness, 200 mm in width, and 100 mm in length for rolling experiments. A binary Mg-Zn alloy modified with Zr was examined as a benchmark alloy. Hot rolling was performed at 400 °C on ZK10, N05, X05, and ZN10 and at 370 °C on ZX10 to the final thickness of 8 mm. The thickness reduction was between 10 to 20% per rolling pass, and the sheets were reheated to the rolling temperature for 600 to 900 s before each rolling step. Different annealing conditions were applied to achieve comparable initial microstructures, as also given in Table 1. The microstructure analysis was conducted by optical microscopy based on mechanically polished surfaces using an oxide polishing suspension (OPS) and an etchant composed of picric acid [13]. Grain sizes were measured by using a liner intercept measurement. The average grain sizes are also collected in Table 1. The annealed sheets have a fully recrystallized and homogeneous microstructure with similar average grain size, as shown in Fig. 1. In the case of ZK10, a small amount of Zr was added as a microstructure controller in order to avoid abnormal grain growth, which is typically found in binary Mg-Zn alloys after thermomechanical processing. Such abnormal grain growth hinders the collection of diffraction patterns with appropriate grain statistics. Besides the effect of Zr on the grain refiner, its impact on the deformation and recrystallization textures is acknowledged to be negligible [6,14].

Table 1
Chemical compositions in wt%, annealing conditions, and average grain sizes of the N05 and X05 as well as their ternary counterparts containing Zn, i.e., ZK10, ZN10, and ZX10.

Alloy	Zn	Zr	Nd	Ca	Mg	Annealing condition	Grain size (μm)
ZK10	1.32	0.13	–	–	Bal.	400 °C for 900 s	27
N05	–	–	0.61	–	Bal.	400 °C for 900 s	23
X05	–	–	–	0.52	Bal.	400 °C for 1800 s	22
ZN10	1.03	–	0.73	–	Bal.	400 °C for 1800 s	23
ZX10	0.91	–	–	0.54	Bal.	370 °C for 900 s	17

2.2. In-situ hard X-ray experiments under tensile loading

Tensile tests were conducted using a universal testing machine (UTM) installed at the High Energy Material Science beamline, HEMS-P07B, at PETRA III (DESY, Hamburg, Germany). Tensile specimens of dog-bone type with a gauge length of 20 mm and a diameter of 4 mm were machined from each sheet parallel to the RD and the TD for tensile tests at an initial strain rate of 1.5×10^{-4} s^{-1} and room temperature (RT). The experimental setup is schematically shown in Fig. 2 (a). High energy synchrotron X-ray radiation allows tracking the diffraction peaks of the investigated materials during deformation. In such an in-situ diffraction experiment, a representative sample volume can be constantly tracked due to the applied transmission geometry. Synchrotron X-ray radiation with a wavelength of 0.142 Å and a beam size of 0.6 × 0.6 mm^2 was used. The beam size used in this study covers approximately 130,000 grains, calculated from the average grain size, and provides sufficient grain statistics to represent overall deformation behavior. Debye-Scherrer diffraction rings were collected at selected strains during the sample rotation of 105° in 3° steps using an area detector (PerkinElmer XRD 1621) with a fast read-out. During the collection of the Debye-Scherrer rings, the applied loading was stopped. The Debye-Scherrer rings were transmuted from area to diffraction pattern by using an open source software Fit2D [15]. The diffraction patterns were used to evaluate the texture and line profile analysis. The texture was recalculated using an open source software MTEX [16].

2.3. Line profile analysis using the CMWP fitting procedure

Convolutional multiple whole profile (CMWP) fitting procedure was used for evaluating the diffraction patterns and the analysis of the dislocation structures. The CMWP analysis allows revealing the activities of particular slip systems distinguished by their Burgers vectors [17,18]. The line profile analysis was carried out using the diffraction patterns integrated over a sample rotation of 24°, denoted as the omega angle, and an azimuth angle of 24° along the Debye-Scherrer ring at the section perpendicular to the loading direction (LD). The transmutation and integration of the detector image to a diffraction pattern is schematically illustrated in Fig. 2 (b). An example of the diffraction pattern used for the line profile analysis is shown in Fig. 2 (c).

The diffraction patterns in Fig. 2 (c) exhibit a peak broadening after 10% strain as a result of plastic deformation by dislocations, planar faults, and size distribution [19]. A classical Williamson-Hall plot of the examined specimens after the deformation shows a nonmonotonic broadening of full width at half maximum (FWHM), as exemplarily shown in Fig. 3, with respect to the diffraction vector, $g = 2\ sin\ \theta/\lambda$, where θ is the diffraction angle and λ is the wavelength. This type of nonmonotonic broadening demonstrates a strong strain anisotropy due to the dislocations [20,21]. In the present study, the dislocations determined by the classical Williamson-Hall plot are accounted as the main factor leading to the peak broadening in the CMWP analysis, whereas planar faults, e.g. twinning, and size distributions are not considered.

In the CMWP fitting procedure, the peak broadening caused by the dislocations is determined based on the mean square strain, $<\varepsilon^2_{g,L}>$, with respect to the diffraction vector, g, and the Fourier variable, L [18,22]. The mean square strain is given as follows:

$$\left\langle \varepsilon^2_{g,L} \right\rangle \cong \frac{\rho \overline{C_{hk.l} b^2}}{4\pi} f(\eta) \quad (1)$$

where

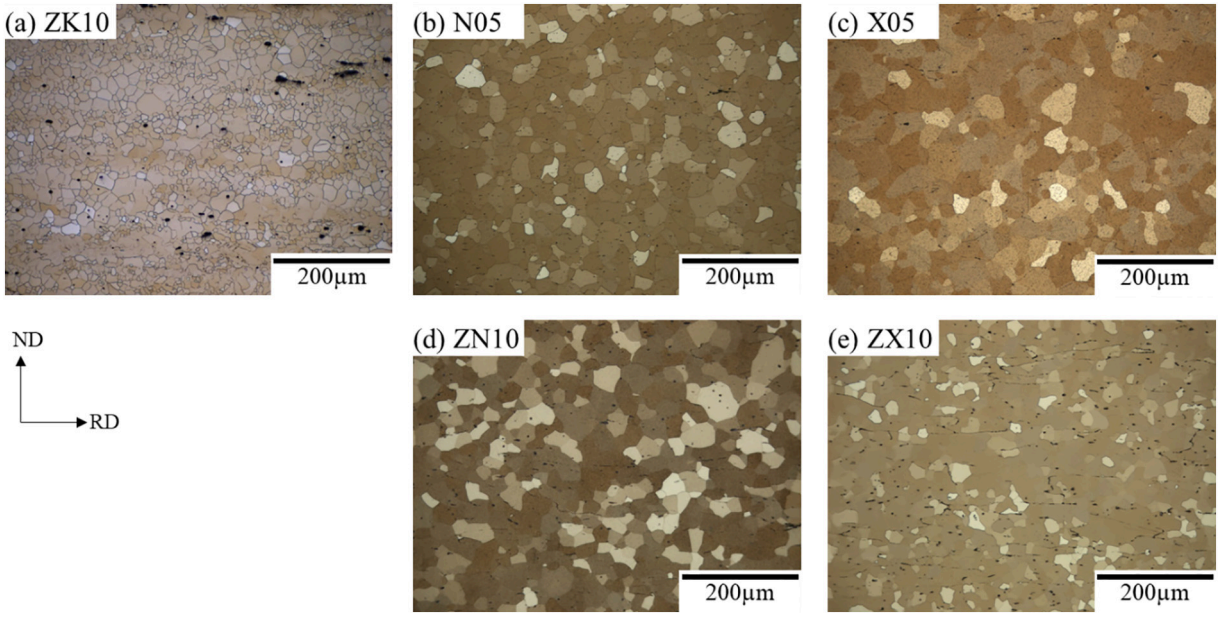

Fig. 1. Initial optical microstructures from longitudinal sections of (a) ZK10, (b) N05, (c) X05, (d) ZN10, and (e) ZX10 sheets after annealing at different conditions.

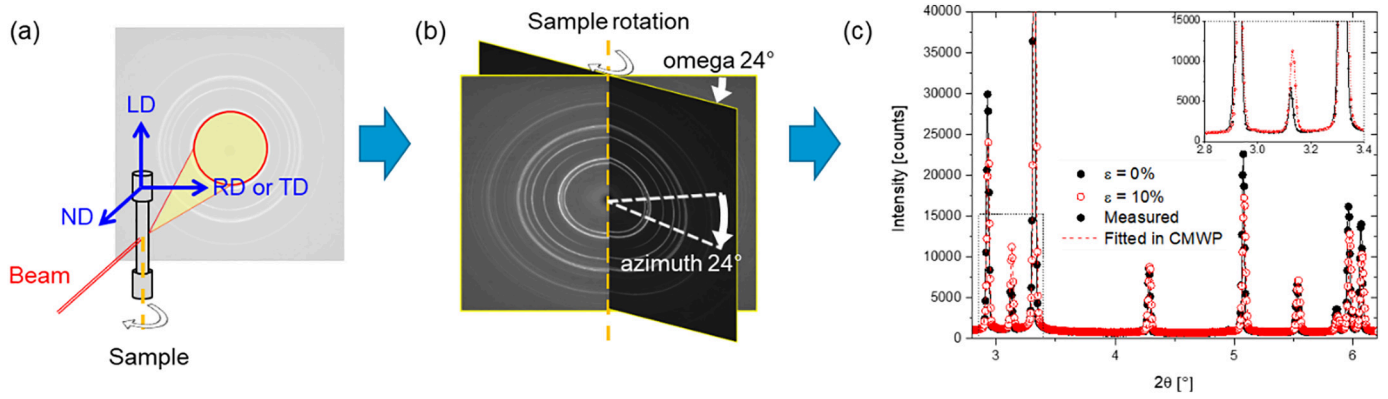

Fig. 2. (a) Sample coordinates in the beamline set-up for in-situ experiments at HEMS-P07B, at PETRA III (DESY, Hamburg, Germany), (b) schematic illustration of the angles of omega and azimuth for the integration from the Debye-Scherrer rings, and (c) transmuted and integrated diffraction patterns at 0% and 10% strain from the in-situ experiment.

$$\overline{C_{hk.l}}b^2 = \sum_{i=1}^{N} f_i \overline{C^i_{hk.l}} b_i^2 \tag{2}$$

ρ is the average dislocation density in the measured volume, and b is the Burgers vector. $f(\eta)$ is the Wilkens function, which eliminates the logarithmic singularity, and $\eta = L/R_e$; R_e is the effective outer cut-off radius of the dislocation. N is the number of different activated sub slip systems. $\overline{C^i_{hk.l}}$ is the average contrast factor corresponding to the ith sub slip systems, and f_i is the fraction of the particular sub slip systems, which contribute to the broadening of a specific reflection. In hexagonal crystals, the average contrast factor has to be extended to consider together with different Burgers vectors, because it is not to have only one type of Burgers vector as in the case of face-centered cubic crystals [19]. The average contrast factor for a single sub slip system in hexagonal crystals is [18].

$$\overline{C_{hk.l}} = \overline{C_{hk.0}}\left[1 + q_1 x + q_2 x^2\right] \tag{3}$$

where $x = (2/3)(1/ga)^2$, q_1 and q_2 are parameters depending on the elastic properties of the material. $\overline{C_{hk.0}}$ is the average contrast factor corresponding to the $hk.0$ type reflections and a is the lattice parameter in the basal plane. The lattice parameters a and c and the corresponding c/a ratio have been determined from the measured $\left(10\bar{1}0\right)$ and (0002) peaks from the synchrotron diffraction measurements for the initial samples in each sheet. They are listed in Table 2. As obviously no difference in the parameters and the ratio is revealed on this diffraction pattern level for the different alloys, the same values for $a = 0.321$ and $c = 0.521$ nm were used for the CMWP fitting procedure and the evaluation of the dislocation density for all examined alloys. It is worthwhile to mention that a potential change of the lattice parameters is also not likely to be found due to the dilute nature of the examined alloys. A potential change of the lattice parameters during deformation was not considered.

The average dislocation density and the experimental parameters q_1 and q_2 (Eq. 3), here denoted as q_1^m and q_2^m as obtained from the peak broadening in the CMWP fitting procedure, are used for the determination of the fractions (weights) of each dislocation type. The fractions of various dislocation types with different Burgers vectors, <a>, <c>, and <c+a>, for all possible combinations were estimated by matching the experimental values (q_1^m and q_2^m) to the theoretical values (q_1^i and q_2^i) in all given slip modes of Mg [17]. The total number of the possible

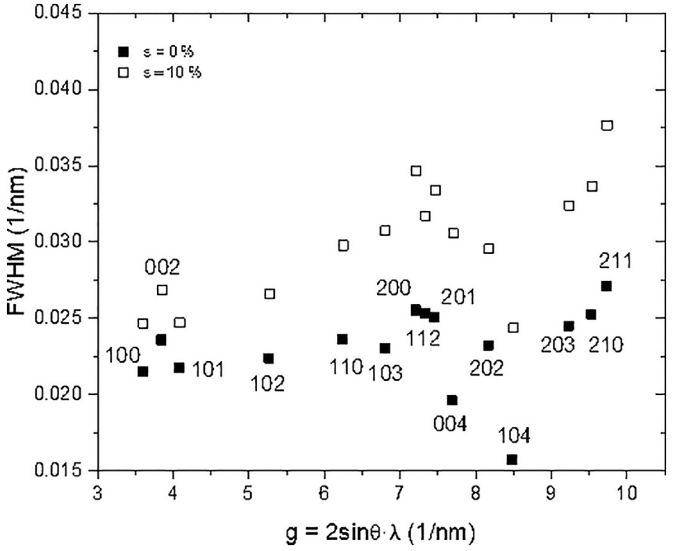

Fig. 3. Example of the classical Williamson-Hall plot of the broadening FWHM at ε = 0% (solid) and 10% (open) of the N05.

Table 2

Lattice parameters a and c and c/a ratio measured using $\left(10\bar{1}0\right)$ and (0002) peaks of the results from the synchrotron diffraction measurement for the initial samples in all examined sheets.

Alloy	a	c	c/a
ZK10	0.3213	0.5215	1.6228
N05	0.3216	0.5218	1.6226
X05	0.3216	0.5218	1.6225
ZN10	0.3213	0.5215	1.6228
ZX10	0.3213	0.5216	1.6231

combinations of different slip systems equals $(2^4-1)(2^2-1)(2^5-1) = 1395$. This repetitive matching is conducted using a computer program, called 'HexBurger'. More detail about the descriptions of the CMWP analysis and the 'HexBurger' program applied in the present study can be found elsewhere [6,18,22]. The q_1^m and q_2^m of the examined sheets after the CMWP fitting are listed in Table 3. The different values are due to the fact that various slip systems are active with different populations in each case.

2.4. IGMA analysis from the EBSD measurement

For electron backscatter diffraction (EBSD) measurement, the tensile specimens deformed up to ε = 10% were prepared by using the same standard preparation techniques with the optical micrograph, which was followed by electrolytic polishing at 33 V and −18 °C for 30 s. The EBSD measurement was conducted on the area of 400 × 400 μm^2 in 0.5 μm step on a field emission gun scanning electron microscope, FE-SEM (Zeiss, Ultra 55 installed with a Hikari detector, EDAX/TSL EBSD system), at an accelerating voltage of 15 kV. In order to reveal the activities of the various dislocations through an intragranular misorientation axis (IGMA) analysis. The IGMA analysis is to evaluate the local misorientation of the crystal lattice with respect to the local axis rotation caused by dislocation slip, which can be determined from the cross product of the slip plane and the slip direction as follows:

$$T_s = n_s \times d_s \tag{4}$$

where T_s, n_s, and d_s are the Taylor axis, slip plane normal, and slip direction, respectively, for given slip modes. According to these assumptions, it is possible to qualitatively determine the dominant slip mode in deformed grains by matching the experimentally measured IGMA to the Taylor axis for a given slip mode. For instance, the prismatic <a> slip accompanies a lattice rotation around the <0001> axis, and the basal <a> and pyramidal <c+a> slip cause a lattice rotation around the $<1\bar{1}00>$ axis as well as the $<10\bar{1}2>$ axis of the pyramidal <a> slip [11,23]. While the analysis method based on a diffraction peak does not include directly available microstructure information, the IGMA

Table 3

The experimental values of the q_1^m and q_2^m fitted by the CMWP analysis in examined sheets.

Alloy	Loading direction		q_1 and q_2 at selected strain levels					
			0.00	0.02	0.05	0.10	0.15	0.20
ZK10	RD	q_1^m	0.696	1.277	1.125	0.614	0.588	0.570
		q_2^m	−0.014	0.022	0.096	0.121	0.112	0.153
	TD	q_1^m	1.653	1.472	0.864	0.547	0.524	–
		q_2^m	−0.117	−0.175	0.174	0.214	0.205	–
N05	RD	q_1^m	1.174	1.044	0.502	0.420	0.339	0.249
		q_2^m	−0.121	−0.067	0.041	0.091	0.124	0.151
	TD	q_1^m	1.853	1.203	0.460	0.359	0.40	0.239
		q_2^m	−0.287	−0.169	0.146	0.137	0.173	0.192
X05	RD	q_1^m	0.670	0.784	0.300	0.228	0.079	–
		q_2^m	−0.049	−0.055	0.026	0.081	0.085	–
	TD	q_1^m	1.971	1.252	0.587	–	–	–
		q_2^m	−0.512	−0.992	0.055	–	–	–
ZN10	RD	q_1^m	0.782	0.507	0.056	−0.002	−0.058	−0.074
		q_2^m	−0.028	0.036	0.051	0.083	0.088	0.09
	TD	q_1^m	1.762	0.964	0.587	0.643	0.315	0.405
		q_2^m	−0.235	−0.078	0.02	0.117	0.109	0.157
ZX10	RD	q_1^m	0.821	0.481	0.099	0.023	0.015	0.030
		q_2^m	−0.032	0.085	0.098	0.113	0.109	0.097
	TD	q_1^m	1.656	0.586	0.331	0.326	0.297	0.291
		q_2^m	−0.23	−0.006	0.063	0.136	0.144	0.155

analysis allows individual grain properties. Especially, this analysis has a benefit of easy identification of the prismatic <a> dislocation slip system in the various dislocation slip activities via the preferred axes of lattice rotation (Taylor axes) within the grains [11,23].

3. Results

3.1. Mechanical properties

The stress-strain curves acquired from the continuous tensile loading at the constant strain rate of all examined sheets along the RD and TD are presented in Fig. 4. Repeated experiments have been stopped at various strain levels for in-situ X-ray measurements. The concurrent stress relaxation during in-situ X-ray measurement has no significant influence on the statistically measurable differences of the active deformation modes and texture evolution from the diffraction experiments, including the flow curve and the work hardening behavior [6,14]. The corresponding tensile properties of the examined sheets are summarized in Table 4. X05 showed a premature fracture at $\varepsilon = 5\%$ during the tensile loading in the TD.

A distinct mechanical anisotropy is observed in the examined alloys. The TD samples in all cases indicate lower yield stress (YS) than those after loading in the RD, while the ultimate tensile stress (UTS) is similar in both loading directions. ZK10 and N05 show a relatively higher YS in both loading directions than X05, ZN10, and ZX10, whereas a higher UTS is observed in the ZK10, ZN10, and ZX10. The difference between the YS and UTS (UTS-YS) can be used to evaluate the work hardening ability. In both loading directions, the larger differences of UTS-YS were measured in ZN10 and ZX10 rather than in N05 and X05, as shown in Table 4. That is, the former has a relatively larger work hardening ability.

3.2. Texture developments

The initial texture of the examined alloys is shown in Fig. 5. While ZK10 shows a strong texture with the c-axis parallel to the ND and no distinct difference of the angular distribution of the basal poles toward the RD or TD, texture weakening is found in the Nd or Ca containing alloys that can be described in two different ways. First, the basal pole split toward the RD is preferentially observed in N05 and X05. Second, the basal pole broadening toward the TD is observed in ZN10 and ZX10. Such texture weakening is known as a result of the addition of RE or Ca in comparison with the conventional Mg alloys, e.g. AZ31 or the ZK10 of the present study [5–7,12,24]. The maximum pole densities of the (0002) pole figures in the examined sheets are $P_{max} = 11$ m.r.d (multiple of random distribution) for ZK10, 5.1 for N05, 5.6 for X05, 2.7 for ZN10, and 3.2 for ZX10, respectively.

Table 4
Tensile properties along the RD and TD measured for the examined sheets at RT (YS: yield strength in MPa, UTS: ultimate tensile strength in MPa, FS: fracture strain).

Alloys	RD loading				TD loading			
	YS	UTS	FS	UTS-YS	YS	UTS	FS	UTS-YS
ZK10	116	190	20	74	107	192	14	85
N05	118	171	31	53	109	170	28	61
X05	105	177	12	72	108	160	5	52
ZN10	113	188	31	75	83	181	23	98
ZX10	109	200	29	91	94	197	24	103

The texture of deformed samples to $\varepsilon = 15\%$ along the RD and TD is shown in Fig. 6. In the case of the TD sample in the X05, the texture measured at $\varepsilon = 5\%$ is presented due to the early fracture. The RD samples of N05 and X05 maintain the RD spread of the basal pole, concurrent with a slight basal pole broadening toward the TD (perpendicular to the LD). The latter is also visible in ZK10. The RD samples of ZN10 and ZX10 clearly indicate a broadening of the basal pole perpendicular to the LD in addition to the basal pole around the ND tilted by 15–20°. Simultaneously, the $<10\bar{1}0>$ pole in the LD strengthens, while the 6 poles at the symmetric position on the $\{10\bar{1}0\}$ pole figure are developed. The TD samples show similar tendencies of the texture development to the RD samples, but with a rotation of 90°, which is the strengthening of the $<10\bar{1}0>$ pole at the LD and the basal pole broadening perpendicular to the LD. Thus, it can be seen that the tendency of the texture development in the examined sheets is qualitatively comparable in both loading directions, but less distinct in the TD samples. It is anticipated that the deformation occurs with identical deformation modes in examined sheets, but different significance.

3.3. Dislocation activities

The activities of the dislocation slip systems during the tensile deformation are evaluated by using the CMWP fitting procedure. The results on the overall dislocation densities as well as the classified

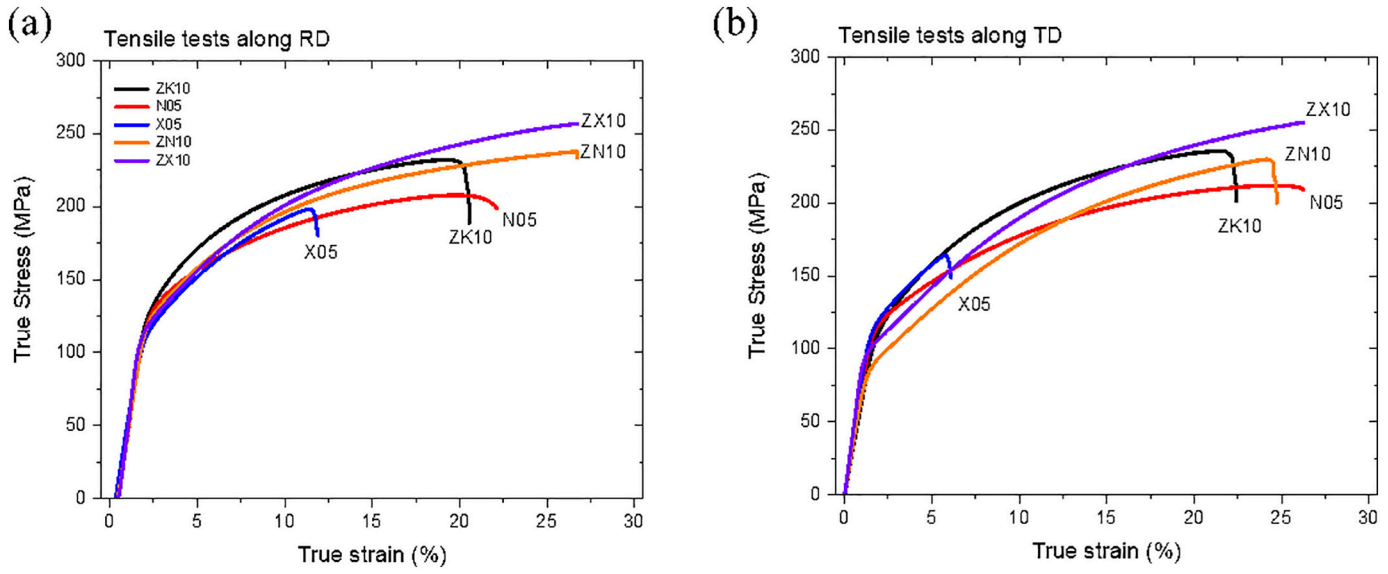

Fig. 4. True stress-true strain curves during the tensile loading along the (a) RD and (b) TD in examined sheets.

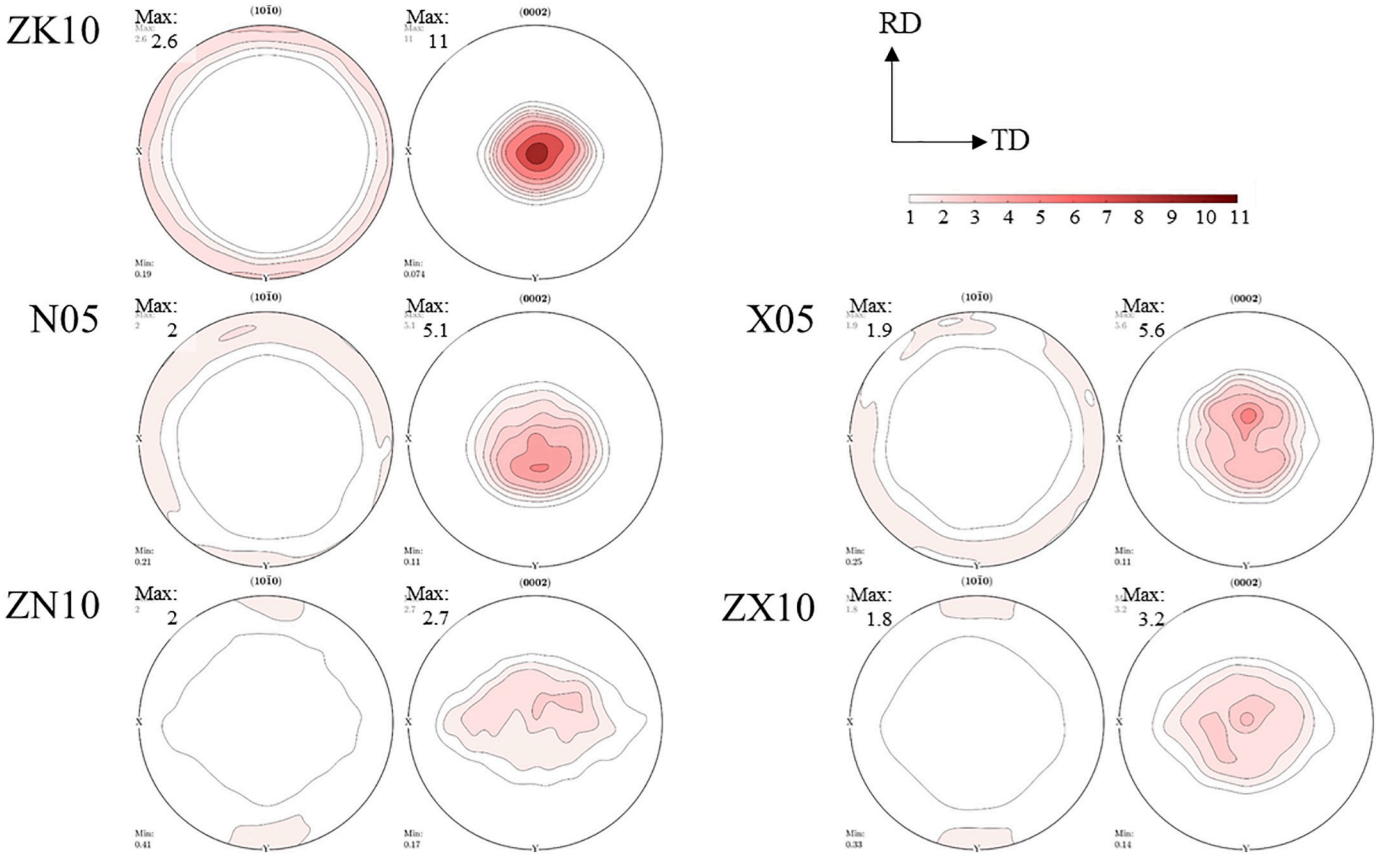

Fig. 5. $\{10\bar{1}0\}$ and (0002) pole figures at annealed condition of the examined sheets (levels: 1.0, 1.5, 2.0, 2.5, 3.0, 4.0, 5.0, 7.0, 9.0, 11.0 m.r.d.).

dislocation densities according to the Burgers vectors are shown in Fig. 7. The X05 sample in the TD is excluded from the detailed evaluation of CMWP analysis, because it is limited to evaluate its tendency of the dislocation activities with only 2% and 5% due to the early fracture (ε = 5% strain). The examined sheets show an increase in the overall dislocation densities with the applied strain in both directions, RD and TD (Fig. 7 (a)). The RD samples of ZN10 and ZX10 show a higher overall dislocation density than those of the TD samples, whereas the other sheets, ZK10, N05, and X05, show no difference in the respective increase comparing both directions. This is associated with the different significance in the dislocation activities for strain accommodation.

This different behavior correlates with the respective activities of <a>, <c>, and <c+a> dislocations, as shown in Figs. 7 (b) and (c). The <a> dislocations play a major role during tensile deformation along both directions, RD and TD, with a fraction higher than 70%. The <c+a> dislocation density then follows with a fraction of 25%, whereas the <c> dislocations have the lowest density (approximately 0.5 × 10^{-14} m^{-2}), which also remains unchanged with increasing strain in all cases. The sheets, except for ZK10, show a comparable development in the activities of the <a> dislocation density at the early stage of deformation up to approximately 5% strain. During the further strain, the increasing tendencies of <a> dislocations vary between the alloys, being the highest in the ZN10 and ZX10, the lowest in N05 and intermediate in X05. The higher densities of the <a> dislocation in the ZN10 and ZX10 are more pronounced in the deformation along the RD, compared to the TD. That is, the <a> dislocations in the ZN10 and ZX10 distinctly increased during the loading in the RD, as shown in Figs. 7 (b) and (c). Consistently, the ZK10 shows the lowest densities of <a> dislocation in both directions. In the case of the densities of <c+a> dislocations, the higher increase in the RD samples of the ZN10 and ZX10 is found. Again, the RD sample of the ZK10 shows the lowest density. In the case of the TD samples, the difference in the densities of the active <c+a> dislocations is relatively low between the alloys. In summary, the higher activation of the <a> and <c+a> dislocations attributes to the higher overall dislocation densities, especially in the RD samples of the ZN10 and ZX10. In comparison between the loading directions, the ZN10 and ZX10 show relatively higher activation of the <a> and <c+a> dislocations during the loading in the RD than in the TD. In the ZK10 and N05, the activities of the <a> dislocations are comparable in both directions, while a slightly higher activation of the <c+a> dislocations is observed in the TD samples than in the RD samples. These differences between the loading directions are associated with the initial texture, corresponding to the 90° rotation of the texture components.

The density evolution of the <a> dislocations, which are the major deformation modes, is evaluated into two separate groups, i.e. basal <a> and nonbasal <a> dislocations. The nonbasal <a> dislocations are considered as a combination of the prismatic and pyramidal edge <a> dislocations because both slip systems cannot be easily distinguished due to their similar peak broadening effects in the X-ray measurement [6,22].

Fig. 8 shows the evolution of the <a> dislocations densities during the deformation along the RD and TD. For both loading directions, the nonbasal <a> dislocations are dominant, whereas a lower basal <a> dislocation density does not change significantly with increasing strain. The remarkable increases of the nonbasal <a> dislocations are indicated in the RD samples of ZN10 and ZX10, which is the highest from all examined cases. This feature is not found in the TD samples. The activation of nonbasal <a> dislocations is shown in N05 and X05. The ZK10 shows the lowest activation of nonbasal <a> dislocations with a similar density evolution in both loading directions. The nonbasal <a> dislocations consistently increase with increasing strain, but their quantities are different for the examined sheets as well as for the loading directions. The differences in the increasing tendencies of nonbasal <a>

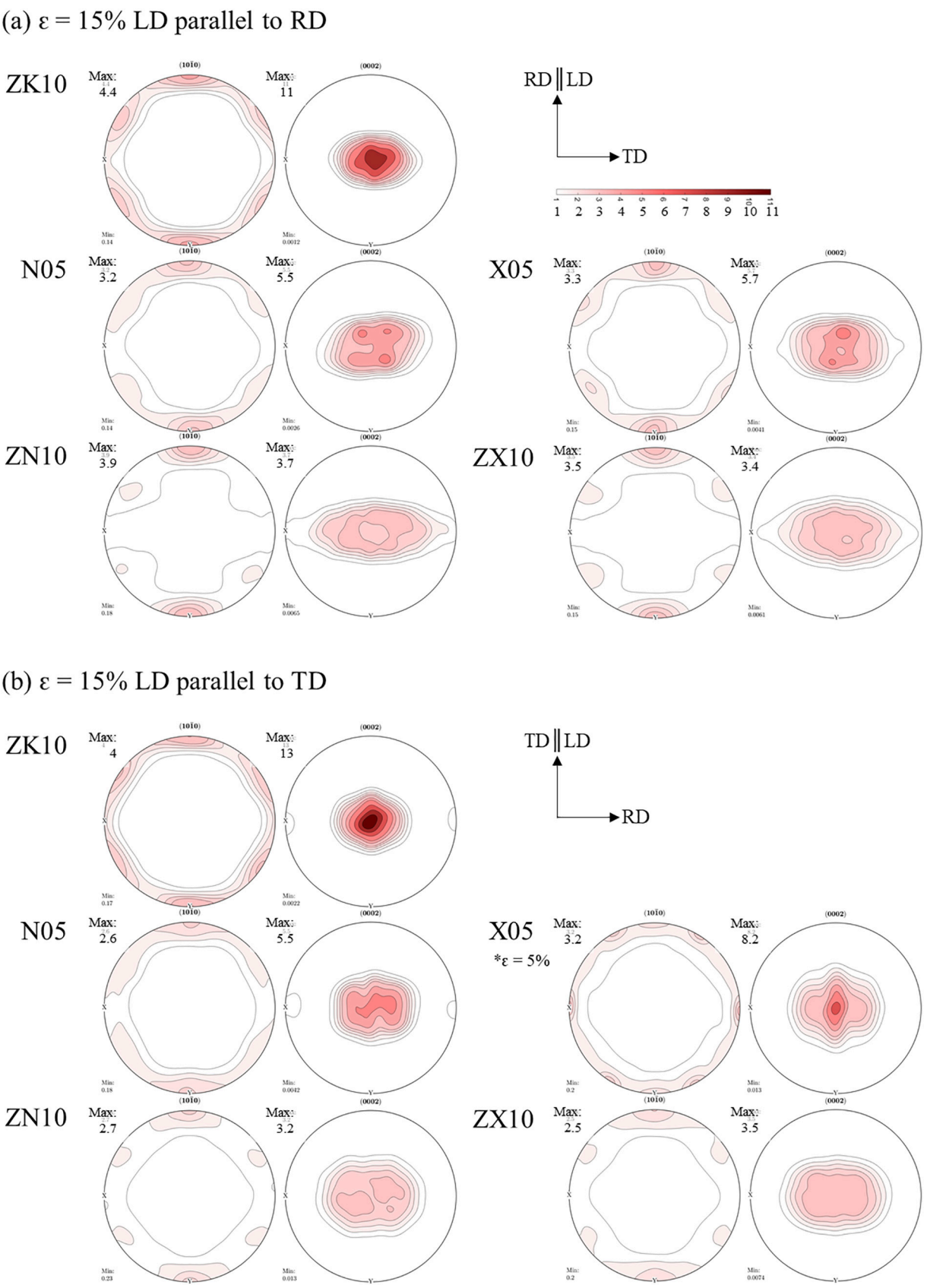

Fig. 6. $\{10\bar{1}0\}$ and (0002) pole figures after deformation, ε = 15%, by the tensile loading along the (a) RD and (b) TD of the examined sheets. The pole figures of the TD samples in the X05 is shown at ε = 5% (Levels: 1.0, 1.5, 2.0, 2.5, 3.0, 4.0, 5.0, 7.0, 9.0, 11.0 m.r.d.).

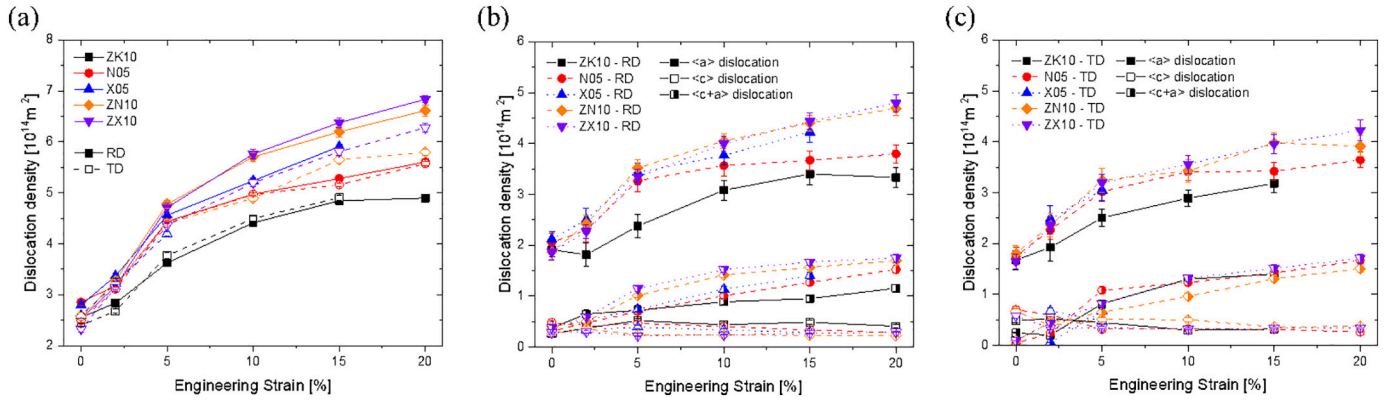

Fig. 7. Evolution of (a) average dislocation density and dislocation density classified according to the three Burgers vectors, <a>, <c>, and <c+a>, along (b) the RD and (c) TD, as a function of applied strain for the examined sheets. The X05 sample in the TD showed the dislocation density at only 2% and 5% due to a premature fracture at $\varepsilon = 5\%$.

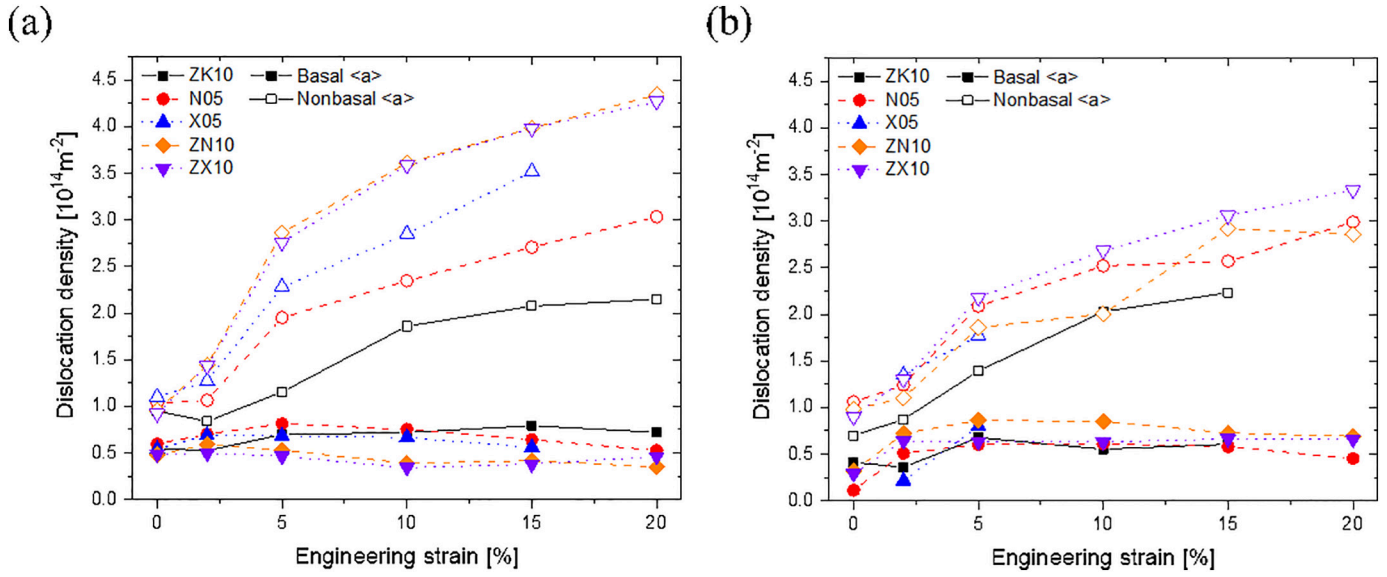

Fig. 8. Dislocation density of the basal edge <a> and nonbasal edge <a> dislocations during deformation along the (a) RD and (b) TD for the examined sheets.

dislocations between the alloys and loading directions relate to the alloying compositions and the initial texture in correlation with Schmid factors. Even though the role of Zn is ambiguous on the activation of nonbasal <a> dislocations, it is obvious that an individual addition of Nd or Ca addition leads to the enhanced activation of nonbasal <a> dislocations in the binary N05 and X05, compared to the ZK10. This finding is in good agreement with a previous study [6]. Moreover, slightly higher basal <a> dislocation densities of ZN10 and ZX10 are found in the TD samples than in the RD samples, while the lower basal <a> dislocations of N05 are found in the TD sample than in the RD sample. Additionally, it is worth mentioning that X05 shows a higher activity of nonbasal <a> dislocations, during the loading in the RD, compared to the N05, as shown in Fig. 8 (a). However, a direct comparison of the efficiency of Nd and Ca for this enhanced activation of nonbasal <a> dislocations is limited due to different contents (0.32 at.% on the Ca and 0.10 at.% on the Nd in binary systems).

3.4. IGMA analysis of the EBSD measurement

Fig. 9 presents representative EBSD orientation maps measured from the tensile samples deformed along the RD up to 10% strain. All EBSD measurements show that homogeneously deformed structures and their microstructures are similar for each sheet except for ZK10, where a locally deformed area, likely shear or deformation band, is visible. The strain accommodation by dislocation glide is reasonably considered. The deformation within a grain results in intergranular misorientation that is visible as colour gradient in the EBSD orientation map. It is noted that the TD sample of X05 was measured after 4% tensile strain due to its premature fracture. An equivalent misorientation angle between 2° and 5° and a grain orientation spread (GOS) higher than 2° are applied to select the deformed grains [6,12,25]. The IGMA analysis allows the determination of the dominating slip systems via the preferred axes of lattice rotation within the grains, so-called Taylor axes [11,23]. Especially the prismatic <a> dislocation slip can be relatively easily identified from the IGMA analysis. Fig. 10 presents the IGMA plots of the deformed grains. The important Taylor axes are marked on the IGMA plot, e.g. $<10\bar{1}0>$ corresponding to basal <a> or pyramidal <c+a> slip, $<10\bar{1}2>$ corresponding to pyramidal <a> slip, as well as <0001> corresponding to prismatic <a> slip [11,23]. For considering the influence of the grain orientation on the dislocation slip, the IGMA plots were determined for two different groups of grain orientations, i.e. one with their c-axes parallel to the ND (RED-grains) and the other with their c-axes perpendicular to the LD (BLUE-grains). The orientations of the grains selected for the IGMA plots are also presented in the (0001) discrete pole figure, Fig. 10.

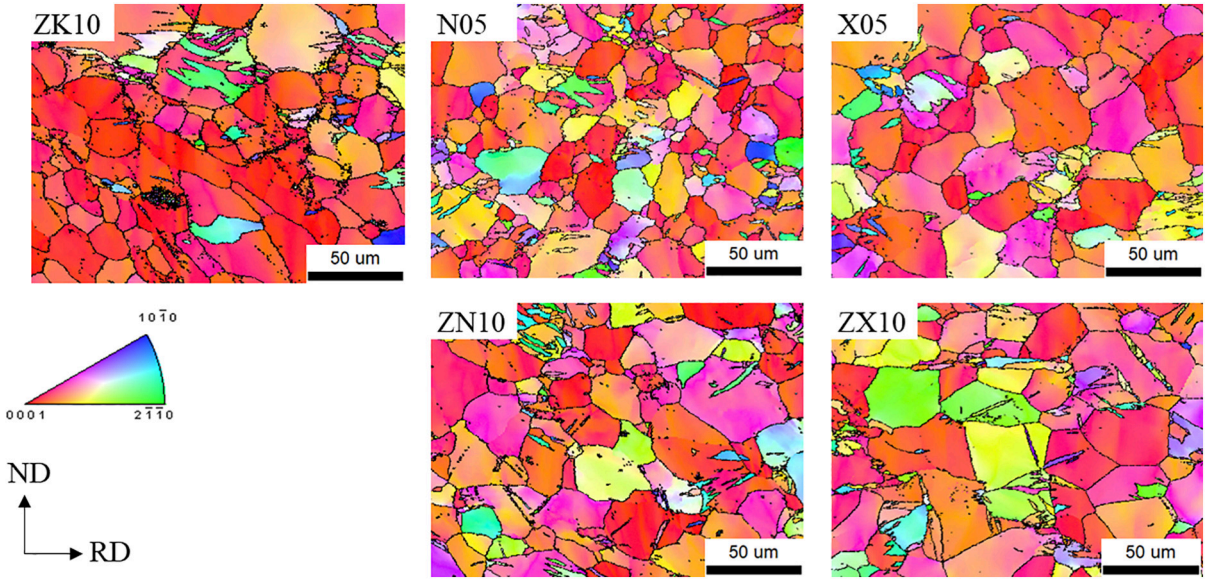

Fig. 9. Representative EBSD orientation maps of the deformed samples along the RD at ε = 10%, for examined sheets. High angle grain boundaries, θ > 15°, are marked with a black line.

In the ZK10, the RED-grains of both RD and TD samples show a concentration of misorientation around the <0001> axis, while the BLUE-grains have a homogeneous distribution of the IGMA. In addition to the concentration at the <0001> axis, ZK10 also shows the relatively high concentration at other axes, compared to the other alloys. This shows that a ratio between prismatic <a> and other slip systems is relatively low, which is in good agreement with the result of the CMWP analysis. In the N05 and X05, the RED-grains of the RD samples show a homogeneous distribution with a slight concentration around the <0001> axis. ZN10 and ZX10 clearly indicate a high concentration of IGMA around <0001> axis, which corresponds to the preferred activity of prismatic <a> slip. Similar behavior is shown in the BLUE-grains, even though they show low grain statistics. On the other hand, the RED-grains of the TD samples in all examined sheets except for the ZK10 indicate a comparable concentration around the <0001> axis of the IGMA plots. That is, the TD samples show small differences in the IGMA distribution between the alloys in comparison with the RD samples. These small differences are visible in the RED- and BLUE-grains of the TD samples. It is a good agreement with the results shown in Fig. 8, where a higher activation of nonbasal <a> dislocations is found in the RD samples for ZN10 and ZX10 rather than for N05 and X05, whereas these differences in the RD samples between the alloys vanish in the TD samples. The other slip systems, which are the basal <a>, pyramidal <a>, and pyramidal <c+a> slip systems, are also activated, but less concentrated in comparison with the prismatic <a> dislocations in the examined sheets except for the ZK10. Moreover, it is worth to mention that the TD sample of the X05 measured at 4% strain also indicates concentration around the <0001> axis. Even though the quantitative analyses, e.g. a direct comparison among the different cases, are difficult, the IGMA results are qualitatively consistent with the results of the CMWP analysis. In other words, the high activation of nonbasal <a> dislocations, measured from the CMWP analysis, is reasonably attributed to the high activity of prismatic <a> slip.

4. Discussion

4.1. The activity of nonbasal dislocation and the texture development

The texture developments of the examined sheets are characterized by the strengthening of the $<10\bar{1}0>$ pole parallel to the LD and a spread of the basal pole perpendicular to the LD, as shown in Fig. 6. All examined sheets show a similar tendency of the texture development irrespective of the initial texture, i.e. loading directions, and alloy compositions. It has been reported in [6,26,27] that the higher activation of the prismatic <a> slip systems leads to such texture development. In the RD samples of N05 and X05, the basal pole spread perpendicular to the LD is slowly formed in comparison to ZN10 and ZX10. These results indicate that the main deformation modes are not different in all examined sheets. However, it seems that different significances of the main deformation modes play a role on the texture development, due to the differences in the initial texture and the addition of alloying elements.

The activity of pyramidal <c+a> dislocation slip is determined in the following order ZK10 < N05 and X05 < ZN10 and ZX10. The pyramidal <c+a> slip is known to lead to the split of the basal pole from the ND toward the LD during deformation [1,28], which is not clearly found in the results obtained from the in-situ texture measurements. The fraction of pyramidal <c+a> dislocation slip measured in the present study is lower than 0.20, which seems not to be sufficient to result in a corresponding texture change. In this regard, it has been reported in [28], that the basal pole split toward the LD formed by the deformation can disappear, if the significance of dominant deformation modes is varied in different loading directions. During the tensile deformation of an AZ31B sheet in the RD and TD, the fractions of prismatic <a> slip were determined as 0.5 and 0.7, respectively, while a similar fraction of about 0.15 was found for the pyramidal <c+a> slip in both directions. Consequently, the texture component of the basal pole split toward the LD disappeared in the TD sample. In addition, it has been reported that a decrease of the CRSS for the activation of pyramidal <c+a> slip requires a higher deformation temperature than 280 °C in Mg alloys, e.g. in AZ31 [29]. In the previous work [6], a higher fraction of pyramidal <c+a> dislocations was observed during the tensile loading at 200 °C in the ZN10 and ZX10, e.g. 0.27 ($\rho_{pyra.}/\rho_{total}$). The corresponding texture change by the pyramidal <c+a> slip system was not observed even at 200 °C, as the nonbasal <a> dislocations were found still dominant [6]. Hence the higher activities of nonbasal <a> slip, especially prismatic <a> slip, and insufficient deformation temperature hinder the formation of the corresponding texture component to the pyramidal <c+a> slip. Nevertheless, it is to mention that the sheets except for ZK10 have the high activation of pyramidal <c+a> dislocation slip (fraction of approximate 0.20), and a weak texture component of basal poles around the ND tilted by 15–20° is formed with increasing strain, e.g. at ε =

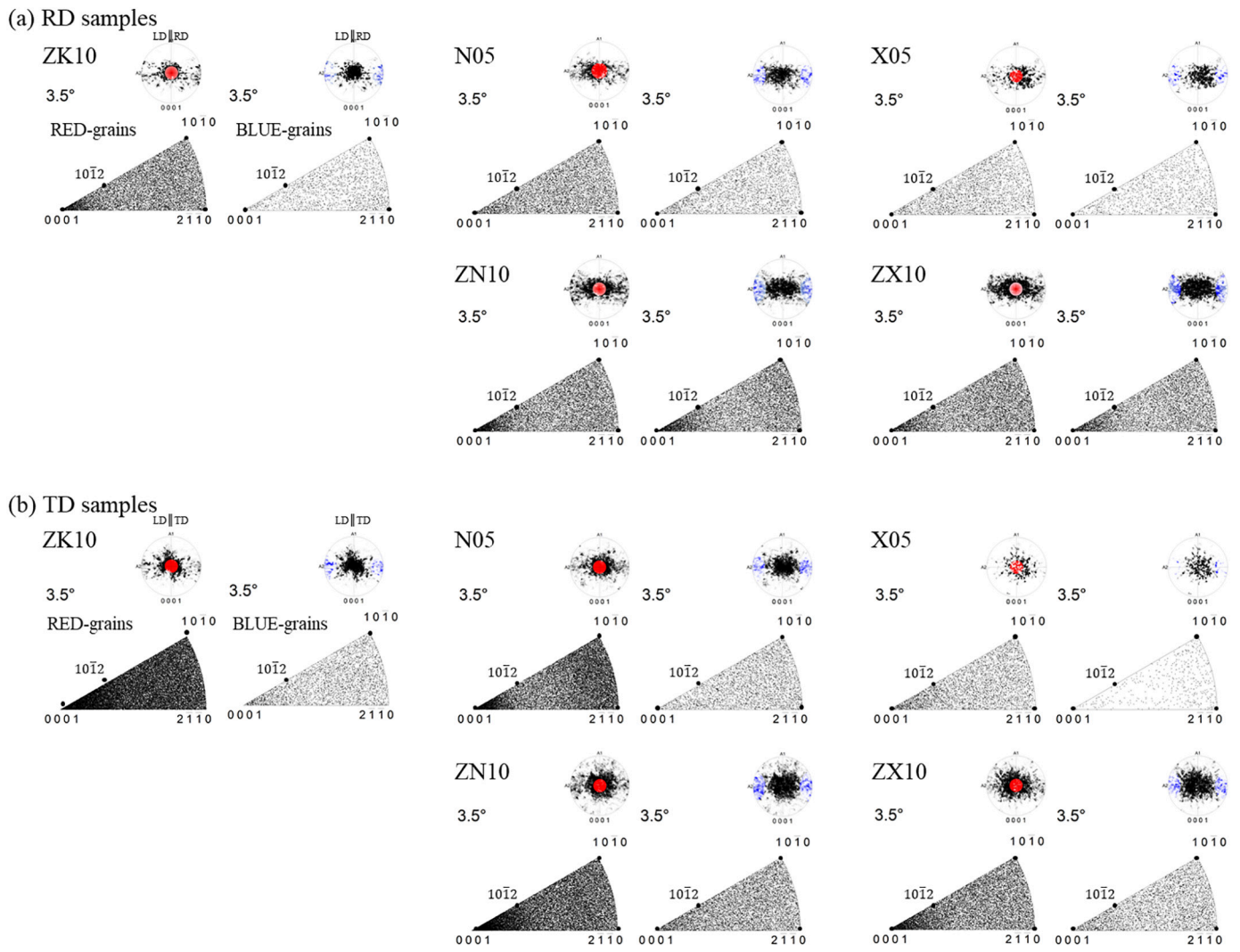

Fig. 10. IGMA plots of the deformed grains (GOS > 2°), depending on the grain orientations (RED- or BLUE-grains), in deformed samples along the (a) RD and (b) TD, at ε = 10% for examined sheets. Exceptively, the TD samples in the X05 showed the IGMA plot at ε = 4%. The (0001) discrete pole figures indicating the orientation of the grains selected for the IGMA analysis are inserted. (For interpretation of the references to colour in this figure legend, the reader is referred to the web version of this article.)

~20%.

It is to mention that the twin behavior is similar in all the examined sheets. The fraction of extension twins is approximately 6–7% in all the examined samples, while the contraction and secondary twins show a low fraction below 1%. However, the texture component corresponding to the extension twin does not represent the global texture development observed from the in-situ texture measurement.

4.2. *Influence of initial texture on the slip activities*

It is revealed that prismatic <a> slip is distinctly active in the Nd or Ca added binary alloys and their counterpart ternary alloys with Zn addition, as confirmed from the CMWP and IGMA results shown in Figs. 8 and 10. It is evident that the Nd or Ca addition enhances the activation of the nonbasal <a> dislocations. Figs. 7 (b) and 8 (a) show that the addition of Zn in combination with the Nd or Ca significantly enhances the activation of prismatic <a> dislocations and pyramidal <c+a> dislocations, especially in the RD samples. High activities of nonbasal dislocations promoted by the Nd or Ca addition also in combination with the Zn result in the distinct texture evolution. The relatively slow evolution of the deformation texture in the N05 and X05 can be understood as a result from the lower activation of prismatic <a> slip, in comparison to ZN10 and ZX10, which matches also to the IGMA analysis of a lower concentration of the Taylor axis around the <0001> axis. The enhancement of the nonbasal <a> dislocations clearly shown in the RD samples diminishes in the TD samples, as shown in Figs. 7 (c) and 8 (b). The influence of the Zn addition should be considered with the contribution of the initial texture to the active deformation modes.

The alloys examined in the present study show characteristic textures after hot rolling and annealing, Fig. 4. The ZK10 forms the basal pole in the ND (no predominant spread toward RD or TD), and the N05 and X05 show the basal pole split toward the RD, whereas the ZN10 and ZX10 indicate a large broadening of the basal pole toward the TD. This provides a higher Schmid factor on the basal <a> slip during the loading in the TD in ZN10 and ZX10. Contrarily, the ZK10, N05, and X05 have a relatively equivalent Schmid factor of the active slip systems in both directions. The CMWP analysis of the ZN10 and ZX10, Fig. 7 (b), indeed indicates that the TD loading induces a higher density of basal <a> dislocations in comparison to the loading in the RD. In the latter case, the activation of basal <a> dislocations is even lower than those of the N05 and X05. The high activity of basal <a> dislocations at early deformation stage, up to ε ~ 5%, in the TD of ZN10 and ZX10 contributes to the relatively small activities of prismatic <a> dislocations and pyramidal <c+a> dislocations, Figs. 7 and 8. Interestingly, during

further loading, the TD samples in the ZN10 and ZX10 do not show a significant increase in the activation of basal <a> dislocations, despite the higher Schmid factor, and nonbasal <a> dislocations become dominant. It is consistent with the mechanical behavior of the low YS in the TD loading of the ZN10 and ZX10, Table 4. This shows that the initial texture itself influences the activity of the slip system at the early deformation stage, but its impact decreases with increasing strain. Conclusively, it is reasonable to consider that the higher activation of nonbasal <a> dislocations, i.e. predominant slip activities, is attributed to the addition of Zn combined with Nd or Ca, rather than the impact of initial texture.

4.3. Influence of alloying elements on the slip activities

It is known that the addition of elements such as Y and Nd results in a significant decrease in the stacking fault energy (SFE) on the basal plane [30,31] and promotes a formation of stacking faults and/or localized segregation during the recrystallization [32]. The reduced SFE on the basal plane in Mg alloys leads to the activation of nonbasal deformation modes, experimentally shown in the present study, because the sessile defect structures (e.g. stacking faults) on the basal plane hinders the dislocation glide on the basal plane. It is assumable that the reduced SFE by the addition of Nd causes a change in the relative critical resolved shear stresses (CRSS) for active slip systems, i.e. an increase of CRSS on basal slip or a decrease of CRSS on prismatic or pyramidal slip systems. Additionally, the stacking fault itself acts as a source of <c+a> dislocations [30,33]. The proposed source mechanism described the formation of pyramidal <c+a> dislocation by the interaction of the active prismatic <a> slip with sessile c dislocation (assuming it exists from the initial stage). Consequently, it can also be understood that prismatic <a> and pyramidal <c+a> slip are highly activated due to the reduction of the SFE and promoting the stacking fault on the basal plane in the present study. The Ca seems to play a similar role in promoting the nonbasal dislocations in Mg alloy.

Furthermore, the presence of Zn added in Mg-Nd and Mg-Ca alloys, ZN10 and ZX10, can be supposed to leading to a higher probability of formation of the stacking fault due to the strong interaction between Zn and Nd or Ca, compared to the individual addition of Nd or Ca. It is recently reported that the phenomenon of combination Zn and Nd or Ca atoms are observed and they have a strong interaction as Zn-Nd or Zn-Ca in Mg alloys than as an individual addition, single Zn, Nd, or Ca [34,35]. Several investigations showed that the SFE decreases distinctly with the simultaneous addition of Y and Zn in comparison with a singular addition of Y [36] and their stacking fault and/or localized segregation tended to form along the (0001) plane [32,37]. Hence, the effective reduction of the SFE by addition of Zn combined with Nd or Ca seems to result in a higher probability of sources for activating nonbasal <a> dislocation slips, which are supported by the present experimental results, i.e. high activations of prismatic <a> and pyramidal <c+a> dislocations, Figs. 6 (b) and 7 (a).

The higher activation of prismatic <a> slip contributes to the aforementioned basal pole broadening perpendicular to the LD. Several studies reported that the texture weakening in Zn containing Mg-RE or Mg-Ca alloy sheets during static recrystallization is accompanied to the TD spread of the basal pole. They revealed that the recrystallization kinetics is retarded due to reduced boundary mobility by co-segregation at grain boundaries and dislocations [32,34,35]. Conclusively, it is supposed that the Zn addition in Mg-RE or Mg-Ca alloys ensures the higher activation of nonbasal <a> dislocation, corresponding to the prismatic <a> slips, relating to the broadened basal pole toward the TD. During recrystallization, this texture component is retained due to the retardation of recrystallization behavior by the presence of Zn, e.g. strong segregation with effectively reduced boundary energy (low boundary mobility) [30,32,35,38].

5. Conclusions

In the present study, in-situ X-ray measurements were applied to investigate the dislocation activities and their impact on the texture evolution under tensile loading in Mg-Nd and Mg-Ca alloys by using the CMWP and IGMA analyses. The addition of Zn in combination with Nd or Ca shows a significant change in the active deformation modes. The main findings from the experimental investigations are concluded as follows:

1. Tensile deformation leads to a strengthening of the $<10\bar{1}0>$ pole parallel to the LD and a spread of the <0001> pole perpendicular to the LD. This tendency of texture development is shown in all cases, irrespective of alloying compositions and loading directions, but its significance is quantitatively different in each alloy.
2. The similarity of texture developments between the examined alloys is anticipated to identical deformation modes activating in all cases. Such texture development is closely related to the high activity of prismatic <a> slip. The CMWP and IGMA analyses have shown the high activities of nonbasal <a> dislocations, especially prismatic <a> slip, while its significances are distinctly different in each alloy.
3. The high activation of prismatic <a> slip is ascribed to the addition of Nd or Ca, compared to the addition of Zn. The addition of Zn combined with Nd or Ca significantly enhances the activation of nonbasal <a> dislocations, including <c+a> dislocations, in comparison with the individual addition of Zn, Nd, and Ca. The quantitatively different texture developments between the examined alloys are attributed to such differences in the activities of the dislocation slip systems by the addition of alloying elements rather than the impact of initial texture.
4. The addition of Zn in combination with Nd or Ca facilitates the development of the basal pole broadening toward the TD during thermomechanical processes due to the enhanced prismatic <a> slip and significant retardation of recrystallization. Contrarily, the individual addition of Zn, Nd, and Ca in Mg does not facilitate the texture development with the formation of TD broadening of the basal pole because there is no significant retardation of recrystallization, even though the enhanced prismatic <a> slips are found.

Data availability

The raw/processed data required to reproduce these findings cannot be shared at this time as the data also forms part of an ongoing study.

Declaration of Competing Interest

The authors declare that they have no known competing financial interests or personal relationships that could have appeared to influence the work reported in this paper.

Acknowledgments

The authors are grateful to Bernd Schwebke at DESY, Günter Meister at HZG and Alexander Reichart at HZG for their technical support. This work was supported by PETRA III at DESY for synchrotron X-ray diffraction experiments. The authors acknowledge funding by the Deutsche Forschungsgemeinschaft (DFG) [grant numbers Bo 2461/4-1, Yi 103/2-1, and BR 961/7-1].

References

[1] S.R. Agnew, M.H. Yoo, C.N. Tome, Application of texture simulation to understanding mechanical behavior of Mg and solid solution alloys containing Li or Y, Acta Mater. 49 (2001) 4277–4289.
[2] J. Bohlen, M.R. Nürnberg, J.W. Senn, D. Letzig, S.R. Agnew, The texture and anisotropy of magnesium–zinc–rare earth alloy sheets, Acta Mater. 55 (2007) 2101–2112.

[3] L. Stutz, J. Bohlen, G. Kurz, D. Letzig, K.U. Kainer, Influence of the processing of magnesium alloys AZ31 and ZE10 on the sheet formability at elevated temperature, Key Eng. Mater. 473 (2011) 335–342.
[4] S.B. Yi, J. Bohlen, F. Heinemann, D. Letzig, Mechanical anisotropy and deep drawing behaviour of AZ31 and ZE10 magnesium alloy sheets, Acta Mater. 58 (2010) 592–605.
[5] X. Zeng, P. Minárik, P. Dobroň, D. Letzig, K.U. Kainer, S. Yi, Role of deformation mechanisms and grain growth in microstructure evolution during recrystallization of Mg-Nd based alloys, Scr. Mater. 166 (2019) 53–57.
[6] C. Ha, J. Bohlen, S. Yi, X. Zhou, H.-G. Brokmeier, N. Schell, D. Letzig, K.U. Kainer, Influence of Nd or Ca addition on the dislocation activity and texture changes of Mg–Zn alloy sheets under uniaxial tensile loading, Mater. Sci. Eng. A 761 (2019) 138053.
[7] T. Al-Samman, X. Li, Sheet texture modification in magnesium-based alloys by selective rare earth alloying, Mater. Sci. Eng. A. Struct. 528 (2011) 3809–3822.
[8] N. Stanford, M.R. Barnett, The origin of “rare earth” texture development in extruded Mg-based alloys and its effect on tensile ductility, Mater. Sci. Eng. A. Struct. 496 (2008) 399–408.
[9] E.A. Ball, P.B. Prangnell, Tensile-compressive yield asymmetries in high-strength wrought magnesium alloys, Scr. Met. Mater. 31 (1994) 111–116.
[10] K. Hantzsche, J. Bohlen, J. Wendt, K.U. Kainer, S.B. Yi, D. Letzig, Effect of rare earth additions on microstructure and texture development of magnesium alloy sheets, Scr. Mater. 63 (2010) 725–730.
[11] J.P. Hadorn, K. Hantzsche, S. Yi, J. Bohlen, D. Letzig, J.A. Wollmershauser, S. R. Agnew, Role of solute in the texture modification during hot deformation of Mg-rare earth alloys, Metall. Mater. Trans. A 43 (2011) 1347–1362.
[12] J. Bohlen, J. Wendt, M. Nienaber, K.U. Kainer, L. Stutz, D. Letzig, Calcium and zirconium as texture modifiers during rolling and annealing of magnesium–zinc alloys, Mater. Charact. 101 (2015) 144–152.
[13] V. Kree, J. Bohlen, D. Letzig, K.U. Kainer, The metallographical examination of magnesium alloys, Prakt Metallogr-Pr M 41 (2004) 233–246.
[14] C. Ha, S. Yi, J. Bohlen, X. Zhou, H.-G. Brokmeier, N. Schell, D. Letzig, K.U. Kainer, Deformation and recrystallization mechanisms and their influence on the microstructure development of rare earth containing magnesium sheets, in: M. Technology (Ed.) TMS 2018 147th Annual Meeting and Exhibition, Phoenix, Arizona, 2018, pp. 209–216.
[15] A.P. Hammersley, Installation europeene de rayonnement synchrotron, in: E.S.R. FACILITY (Ed.) ESRF Internal Report, 2004.
[16] F. Bachmann, R. Hielscher, H. Schaeben, Texture analysis with MTEX – free and open source software toolbox, Solid State Phenom. 160 (2010) 63–68.
[17] I.C. Dragomir, T. Ungar, Contrast factors of dislocations in the hexagonal crystal system, J. Appl. Crystallogr. 35 (2002) 556–564.
[18] K. Mathis, K. Nyilas, A. Axt, I. Dragomir-Cernatescu, T. Ungar, P. Lukac, The evolution of non-basal dislocations as a function of deformation temperature in pure magnesium determined by X-ray diffraction, Acta Mater. 52 (2004) 2889–2894.
[19] T. Ungar, J. Gubicza, G. Ribarik, A. Borbely, Crystallite size distribution and dislocation structure determined by diffraction profile analysis: principles and practical application to cubic and hexagonal crystals, J. Appl. Crystallogr. 34 (2001) 298–310.
[20] T. Ungár, A. Borbély, The effect of dislocation contrast on X-ray line broadening: a new approach to line profile analysis, Appl. Phys. Lett. 69 (1996) 3173–3175.
[21] M. Wilkens, The determination of density and distribution of dislocations in deformed single crystals from broadened X-Ray diffraction profiles, Phys. Status Solidi A 2 (1970) 359–370.
[22] K. Mathis, G. Csiszar, J. Capek, J. Gubicza, B. Clausen, P. Lukas, A. Vinogradov, S. R. Agnew, Effect of the loading mode on the evolution of the deformation mechanisms in randomly textured magnesium polycrystals – Comparison of experimental and modeling results, Int. J. Plast. 72 (2015) 127–150.
[23] Y.B. Chun, M. Battaini, C.H.J. Davies, S.K. Hwang, Distribution characteristics of in-grain misorientation axes in cold-rolled commercially pure titanium and their correlation with active slip modes, Metall Mater Trans A 41 (a) (2010) 3473–3487.
[24] L. Mackenzie, M. Pekguleryuz, The recrystallization and texture of magnesium–zinc–cerium alloys, Scr. Mater. 59 (2008) 665–668.
[25] J. Victoria-Hernandez, S. Yi, J. Bohlen, G. Kurz, D. Letzig, The influence of the recrystallization mechanisms and grain growth on the texture of a hot rolled AZ31 sheet during subsequent isochronal annealing, J. Alloys Compd. 616 (2014) 189–197.
[26] S.R. Agnew, O. Duygulu, A mechanistic understanding of the formability of magnesium: examining the role of temperature on the deformation mechanisms, Mater. Sci. Forum 419-4 (2003) 177–188.
[27] J. Koike, T. Kobayashi, T. Mukai, H. Watanabe, M. Suzuki, K. Maruyama, K. Higashi, The activity of non-basal slip systems and dynamic recovery at room temperature in fine-grained AZ31B magnesium alloys, Acta Mater. 51 (2003) 2055–2065.
[28] S.R. Agnew, Ö. Duygulu, Plastic anisotropy and the role of non-basal slip in magnesium alloy AZ31B, Int. J. Plast. 21 (2005) 1161–1193.
[29] M.R. Barnett, A Taylor model based description of the proof stress of magnesium AZ31 during hot working, Metall Mater Trans A 34 (a) (2003) 1799–1806.
[30] S. Sandlöbes, M. Friák, S. Zaefferer, A. Dick, S. Yi, D. Letzig, Z. Pei, L.F. Zhu, J. Neugebauer, D. Raabe, The relation between ductility and stacking fault energies in Mg and Mg–Y alloys, Acta Mater. 60 (2012) 3011–3021.
[31] S. Sandlöbes, Z. Pei, M. Friák, L.F. Zhu, F. Wang, S. Zaefferer, D. Raabe, J. Neugebauer, Ductility improvement of Mg alloys by solid solution: Ab initio modeling, synthesis and mechanical properties, Acta Mater. 70 (2014) 92–104.
[32] Y.M. Kim, C. Mendis, T. Sasaski, D. Letzig, F. Pyczak, K. Hono, S.B. Yi, Static recrystallization behaviour of cold rolled Mg-Zn-Y alloy and role of solute segregation in microstructure evolution, Scr. Mater. 136 (2017) 41–45.
[33] M.H. Yoo, S.R. Agnew, J.R. Morris, K.M. Ho, Non-basal slip systems in HCP metals and alloys: source mechanisms, Mater. Sci. Eng. A. Struct. 319 (2001) 87–92.
[34] M. Sanjari, A.R. Farkoosh, B. Shalchi Amirkhiz, Y. He, A. Javaid, A.S. Kabir, J. Su, I.-H. Jung, S. Yue, The role of the Zn/Nd ratio in the microstructural evolution of the Mg-Zn-Nd system during static recrystallization: grain boundary partitioning of solutes, Scr. Mater. 134 (2017) 1–5.
[35] Z.R. Zeng, Y.M. Zhu, S.W. Xu, M.Z. Bian, C.H.J. Davies, N. Birbilis, J.F. Nie, Texture evolution during static recrystallization of cold-rolled magnesium alloys, Acta Mater. 105 (2016) 479–494.
[36] Q. Zhang, L. Fu, T.-W. Fan, B.-Y. Tang, L.-M. Peng, W.-J. Ding, Ab initio study of the effect of solute atoms Zn and Y on stacking faults in Mg solid solution, Phys. B Condens. Matter 416 (2013) 39–44.
[37] D. Egusa, E. Abe, The structure of long period stacking/order Mg–Zn–RE phases with extended non-stoichiometry ranges, Acta Mater. 60 (2012) 166–178.
[38] M. Yuasa, M. Hayashi, M. Mabuchi, Y. Chino, Improved plastic anisotropy of Mg–Zn–Ca alloys exhibiting high-stretch formability: a first-principles study, Acta Mater. 65 (2014) 207–214.